

## KEPLER FLARES III: STELLAR ACTIVITY ON GJ 1245 A AND B

JOHN C. LURIE<sup>1</sup>, JAMES R. A. DAVENPORT<sup>1</sup>, SUZANNE L. HAWLEY<sup>1</sup>, TESSA D. WILKINSON<sup>1</sup>, JOHN P. WISNIEWSKI<sup>2</sup>,  
ADAM F. KOWALSKI<sup>3</sup>, AND LESLIE HEBB<sup>4</sup>

*Draft version September 16, 2018*

### ABSTRACT

We present the flare occurrence rates and starspot evolution for GJ 1245 A and B, two active M5 stars, based on nine months of Kepler short cadence observations, and four years of nearly continuous long cadence observations. The A component is separated from the B component by  $7''$ , and the stars are not resolved in the Kepler pipeline processing due to Kepler's large plate scale of  $4''/\text{pixel}$ . Analyzing the target pixel data, we have generated separate light curves for components A and B using the PyKE pixel response function modeling procedures, and note the effects of CCD saturation and non-linear response to high energy flares. In our sample, GJ 1245A and B exhibit an average of 3.0 and 2.6 flares per day, respectively. We introduce a new metric,  $L_{fl}/L_{Kp}$ , to compare the flare rates between stars, and discuss this in the context of GJ 1245 A and B. Both stars exhibit starspot features that evolve on long time scales, with the slower rotating B component showing evidence of differential rotation. Intriguingly, the angular separation between the A and B component photocenters decreases during the four years of observations in a manner consistent with a shift in the position of the A photocenter due to the orbit of its unseen M8 companion (GJ 1245C), which is  $\sim 94\%$  less bright. Among the most detailed photometric studies of fully convective M dwarfs in a multiple system, these results provide an important constraint on stellar age-rotation-activity models.

*Keywords:* stars: low mass; stars: activity; techniques: image processing

### 1. INTRODUCTION

The magnetic fields of M dwarfs manifest themselves in several observable ways. These include flares (e.g. Lacy et al. 1976), starspots (e.g., Contadakis 1995; McQuillan et al. 2014), chromospheric H $\alpha$  emission (e.g., Hawley et al. 1996), and X-ray emission (e.g., Güdel 2004). There has been a longstanding effort to tie such observables to the internal magnetic dynamo, and to disentangle the interdependent effects of stellar mass, age, and rotation rate. In the age-rotation-activity paradigm (e.g., Skumanich 1972), activity depends on rotation rate, which in turn depends on age. Complicating matters, M dwarfs become fully convective at approximately type M4 (Chabrier & Baraffe 1997), and thus do not have a Solar-like dynamo. While models indicate that activity in fully convective stars depends on rotation rate (Dobler et al. 2006; Browning 2008), there is observational evidence for a rotation threshold (Delfosse et al. 1998; Mohanty & Basri 2003; Browning et al. 2010), above which activity no longer correlates with rotation rate.

Because they are coeval, stars in multiple systems provide a control for age, and are test cases for the age-rotation-activity paradigm. Among the nearest (4.5 pc; van Altena et al. 1995) and brightest M dwarfs in the Kepler dataset, the GJ 1245 system is comprised of two active M5 components (A and B), and an M8 companion (C) to A. The spectral types reported here are those in Hawley et al. (2014), hereafter referred to as Paper 1. At

$\sim 3$  magnitudes fainter (94% less bright) than component A, component C does not contribute significantly to the total quiescent flux in the Kepler bandpass. Kepler has observed flares on stars as late as L1 (Gizis et al. 2013), and it is possible that a flare on component C could be detected and mistakenly assigned to component A. We discuss the contribution of the C component to our flare sample uncertainties in §4. For simplicity, we refer to the properties of the A component individually unless otherwise noted, but the Kepler observations presented here are of the combined flux from the A and C components.

The A and C components are separated by  $\sim 0''.6$  (2.7 AU) (Dieterich et al. 2012) with an orbital period of  $\sim 15$  years (Harrington 1990), while the AC and B components are separated by  $\sim 7''$  (32 AU), with an estimated orbital period of 330 years assuming a circular orbit and a total system mass of  $0.3 M_{\odot}$  (Harrington 1990). As discussed in §2.3.1, we see the separation between the photocenters of the AC and B components decrease during the 4 years of Kepler observations in a manner that is consistent with the orbit of the AC system. Due to Kepler's large plate scale of  $4''/\text{pixel}$ , separate light curves for components A and B cannot be generated by aperture photometry. That limitation motivated this work, which aims to generate separate light curves for components A and B from the pixel-level data.

This paper is the third in a series studying flares with Kepler. Paper 1 examined the stellar activity of 5 early-to-mid type M dwarf systems, including GJ 1245. Paper 1 reported the rotation periods for components A and B of  $0.2632 \pm 0.0001$  and  $0.709 \pm 0.001$  days, respectively, based on light curve modulations due to starspots. We confirm those periods within the uncertainties, which are likely due to the effects of differential rotation discussed in §3. Paper 1 also reported a flare sample for the AB system, based on their combined light curve. Davenport

<sup>1</sup> Department of Astronomy, University of Washington, Seattle, WA 98195, USA; [lurie@uw.edu](mailto:lurie@uw.edu)

<sup>2</sup> HL Dodge Department of Physics & Astronomy, University of Oklahoma, Norman, OK 73019, USA

<sup>3</sup> NASA Goddard Space Flight Center, Greenbelt, MD 20771, USA

<sup>4</sup> Department of Physics, Hobart and William Smith Colleges, Geneva, NY 14456, USA

et al. (2014), hereafter referred to as Paper 2, focused on the active M dwarf GJ 1243, with a detailed analysis of the temporal morphology of its flares based on a sample of over 6,100 flare events. In this paper, we analyze the flare properties and starspot evolution of the two stars individually based on their separated light curves.

Containing two nearly identical and fully convective M dwarfs, the GJ 1245 system provides a unique test case to break some of the degeneracies in stellar age-rotation-activity models. Given that stars A and B are coeval and of nearly equal mass, but have rotation periods that differ by almost a factor of 3, we aim to answer several simple yet fundamental questions. Namely, which star flares more often, and how do the energy distributions of their flares differ? We introduce a new metric,  $L_{fl}/L_{bol}$ , to compare the energy emitted in flares relative to the bolometric luminosity, and discuss the caveats of this metric in the context of GJ 1245 A and B. As both stars exhibit periodic brightness variations due to starspots, we also aim to determine if their starspot properties differ, and look for evidence of differential rotation. Here we are interested in the bulk activity properties of the two stars, and their dependence on rotation rate.

The outline of the paper is as follows. In section §2 we describe the Kepler data, demonstrate that they contain a clear signal from both components A and B, and describe the process used to generate separate light curves for each component. In §3 we compare the nature and evolution of their starspots, and in §4 we identify and compare the flares on each component. We conclude in §5 by comparing these results to those for GJ 1243, and discuss the results in the broader context of stellar age-rotation-activity models.

## 2. OBSERVATIONS AND ANALYSIS

The analysis presented here involves Kepler target pixel files, which contain the raw data transmitted from the spacecraft. A full description of Kepler data processing is given in Fanelli et al. (2011), but we give a brief overview. The Kepler detector consists of 42 CCDs, each of which is divided in half to create 84 output channels. Due to onboard storage and transmission limitations, Kepler was unable to transmit the full image of its field of view with every exposure. Instead, only the pixels immediately surrounding targets, referred to as target pixel masks, or “postage stamps”, were transmitted. A target pixel file contains all of the images of a mask taken during an observing quarter. For each mask, an aperture around the target was chosen. The pixels within this aperture were used in the Kepler Science Operations Center processing to produce the calibrated, detrended Pre-search Data Conditioning - Simple Aperture Photometry (PDC-SAP) light curve (Smith et al. 2012). The PDC-SAP light curves were used for the bulk of the Kepler exoplanet investigations, as well as the stellar activity analyses in Papers 1 and 2. In this section we present our justification for performing our own reduction using PyKE pixel response function (PRF) fitting models, as well as the validation of those models.

### 2.1. Kepler Target Pixel Files

The GJ 1245 system was observed with two different pixel masks. Component A (KIC 008451868) was targeted in long cadence mode (30 minute sampling) during

quarters 1 – 17 under Guest Observer programs 10000 and 20028. Component B (KIC 008451881) was targeted in long cadence mode during quarters 0 – 17, and in short cadence mode (1 minute sampling) during quarters 8, 10, and 11 under Guest Observer programs 20016, 20028, 20031, and 30002. Each quarter corresponds to approximately three months of observations, with the exception of quarters 0, 1, and 17, which are shorter. While observed as separate objects, the target pixel files are similar and contain both components within the masks. However, the PDC-SAP light curves are very different because in each case the apertures were chosen to minimize the flux from the other component. The analysis in Paper 1 used the B component data, as the short cadence observations were taken with that mask.

The PDC-SAP light curves exhibit flares and periodic modulation due to starspots. As reported in Figure 4 of Paper 1, a periodogram of the light curve from the B component mask reveals two strong signals at 0.26 and 0.71 days corresponding to the rotation periods of components A and B, respectively. The light curve from the A component pixel mask does not contain any significant signal at the rotation period of the B component, likely because the aperture and data reduction removed most of the B component flux. The PDC-SAP light curve for the B component presents a challenge, as it was taken in the short cadence mode most sensitive to flares, but contains significant signal from star A. Using these data, it is impossible to determine which component is flaring, and to compare the starspot evolution of each component individually.

This limitation motivated us to examine the target pixel files with the hope of generating separate, uncontaminated light curves for each component. We focused our analysis on the B component pixel mask data, as it included short cadence observations that are necessary to detect all but the largest energy flares. The data are stored as FITS files containing the observation time, the raw counts in each pixel, and the calibrated flux in each pixel. While this calibration includes corrections such as bias subtraction and flat fielding, it does not remove systematic instrumental trends, unlike the PDC-SAP processing. The target pixel files also contain information such as the aperture boundaries, the World Coordinate System (WCS) transformations, and the instrument configuration. In the case of GJ 1245, the size of the mask region ranged in size from  $7 \times 8$  pixels to  $13 \times 11$  pixels. The Kepler detector has a large plate scale of  $4''/\text{pixel}$ , undersampling its PSF and producing images that can initially be challenging to interpret. Given the relatively small number of pixels involved, we found it most effective to plot the fluxes contained in each pixel as individual light curves.

An example plot of 1.5 days of Quarter 8 short cadence data is shown in Figure 1. The plot contains spatial, temporal, and frequency information. The  $11 \times 10$  grid represents the spatial extent of the pixel mask, with each cell corresponding to one pixel. The field of view is shown by the arrow labeled  $44''$  at the top of the plot. Arrows labeled “N” and “E” in the bottom left corner show the on-sky orientation of the mask. Within each pixel, flux is on the y-axis with a range of  $2,000 \text{ e}^- \text{ s}^{-1}$ , and time is on the x-axis with a range of 2.0 days, as noted in the lower left corner. Only 1.5 days of data are shown for

visual clarity. For reference, the boundary of the PDC-SAP aperture is outlined in green. As discussed in §2.2, the locations of the PRF model sources for the A and B components are shown as a yellow circle and X, respectively. The expected positions of the stars based on their R.A. and decl. are plotted as a yellow open square and plus symbol, respectively. The R.A. and decl. are obtained from the targets’ 2MASS coordinates (Cutri et al. 2003) precessed to epoch J2000.0, taking into account the proper motions in Harrington (1990). The resulting coordinates were converted to pixel locations using the WCS transformations contained in the target pixel files.

The pixel-level data contain two clear periodic signals corresponding to the two rotation periods. Pixels have been colored based on the strength of the signal from each component, i.e., the power of the peaks in the periodogram for that pixel. Red pixels contain a 0.26 day signal from the A component, while blue pixels contain a lower amplitude 0.71 day signal from the B component. Purple pixels in the center contain signal from both components, as evidenced by the beat pattern. White pixels are sky pixels and do not contain a significant signal from either component. During this time period there is a flare on the B component pixels that does not appear on the A component pixels. This plot demonstrates both the wealth of information contained in the target pixel files, and the feasibility of generating separate light curves to recover individual information on starspot modulation and flares for each component.

While the two stellar components are clearly evident in the pixel-level data, they are not separated enough in the images to generate uncontaminated light curves via aperture photometry. We note that the aperture used for the B component PDC-SAP reduction, outlined in green in Figure 1, largely excludes pixels of the A component. This was done consistently for all quarters across the entire observation period, thus eliminating a large fraction of the total flux from the system. This explains the observation made in Paper 1 that the PDC-SAP light curve was unexpectedly noisy given the total brightness of the GJ 1245 system. However, as the B component PDC-SAP light curve still contains a significant signal from the A component, it is of limited utility in studying the flare and starspot properties of the B component individually.

## 2.2. PRF Model Light Curves with PyKE

To generate separate light curves for each component, we used the *keprf* and *keprfphot* routines in the PyKE software package (Still & Barclay 2012). Full documentation of PyKE is available on the Kepler Guest Observer website<sup>5</sup>. The *keprf* routine fits one or more sources to a target pixel image, using a PRF model derived during spacecraft commissioning. The *keprfphot* routine performs the same functions as *keprf*, but generates light curves by fitting the observations within a given time window, or an entire quarter. Here we make a distinction between the point spread function (PSF), which is how light falls onto the detector, and the PRF, which is how the detector sees the PSF. The PRF can differ from the PSF due to pointing jitter during an exposure and systematics within the detector.

The Kepler PRF model was derived during spacecraft commissioning by observing approximately 19,000 calibration stars in a dither pattern (Bryson et al. 2010). This dithering allowed the PRF to be sampled at the sub-pixel level. The PRF model was then computed as a polynomial fit to the dithered observations. The publicly available PRF model used by PyKE is in the form of a lookup table. For each CCD output channel, there are five PRF models, one defined at each corner and one in the center. The PyKE routines linearly interpolate between the five PRF models to generate a single model used for the fit. The model is defined on a  $50 \times 50$  grid within each pixel. Given three user-specified free parameters for the sources: flux and the column and row positions on the detector, the routines use the PRF model to compute the total flux within the mask that would result from sources with the given locations and fluxes. They then find the parameters that minimize the residual flux across the pixel mask.

As the locations of the components on the detector vary from quarter to quarter due to spacecraft roll and pointing changes, we first ran *keprf* to determine their initial locations at the start of each quarter. Knowing the on-sky separation of the two components, and using the rotation period information seen in Figure 1, we were able to make a reasonable guess of the source locations. As stated in the PyKE documentation, the model convergence is not very dependent on the initial guesses for location, as long as they are within one pixel of the true position. Because the components are of roughly equal luminosity, we set the initial fluxes to equal. Convergence of the model is also not very dependent on the initial flux values.

A typical output of the *keprf* routine is shown in Figure 2. The top left panel shows an image from the same quarter and pixel mask as Figure 1. Unlike Figure 1, the greyscale color bar signifies the flux for a single exposure. The top right panel shows the PRF model with sources at the A and B component locations. The locations of the A and B components in the model are shown as the yellow circle and X, respectively, in Figure 1. The model flux is defined on a  $50 \times 50$  sub-pixel grid, which must be summed within each pixel to generate the pixel-level fluxes labeled “Fit” in the lower left panel. The residuals between the observation and the fit are shown the lower right panel. Note that the color bar for this residual panel contains both negative and positive values, and has a factor of 10 smaller range in order to show the residuals in greater contrast. We analyze the residuals and validate the PRF model in §2.3.3.

In our reduction, we chose to include exposures flagged with quality issues, as described in the Kepler Archive Manual (Thompson & Fraquelli 2014). Generally representing  $\lesssim 10\%$  of the data in a given quarter, some of these flagged observations are not in fact exposures, but instead placeholders for when the spacecraft was in safe mode, and thus contain no data. In this case *keprfphot* does not attempt a fit. Some exposures were flagged as containing a cosmic ray. If a genuine cosmic ray were detected, it would be limited to a single exposure and therefore not identified as a flare by the procedure described in §4. It is also possible that a genuine flare event could be mistaken for an anomaly and removed in the calibration of the target pixel files, but the data flags

<sup>5</sup> [keplergo.arc.nasa.gov/PyKE.shtml](http://keplergo.arc.nasa.gov/PyKE.shtml)

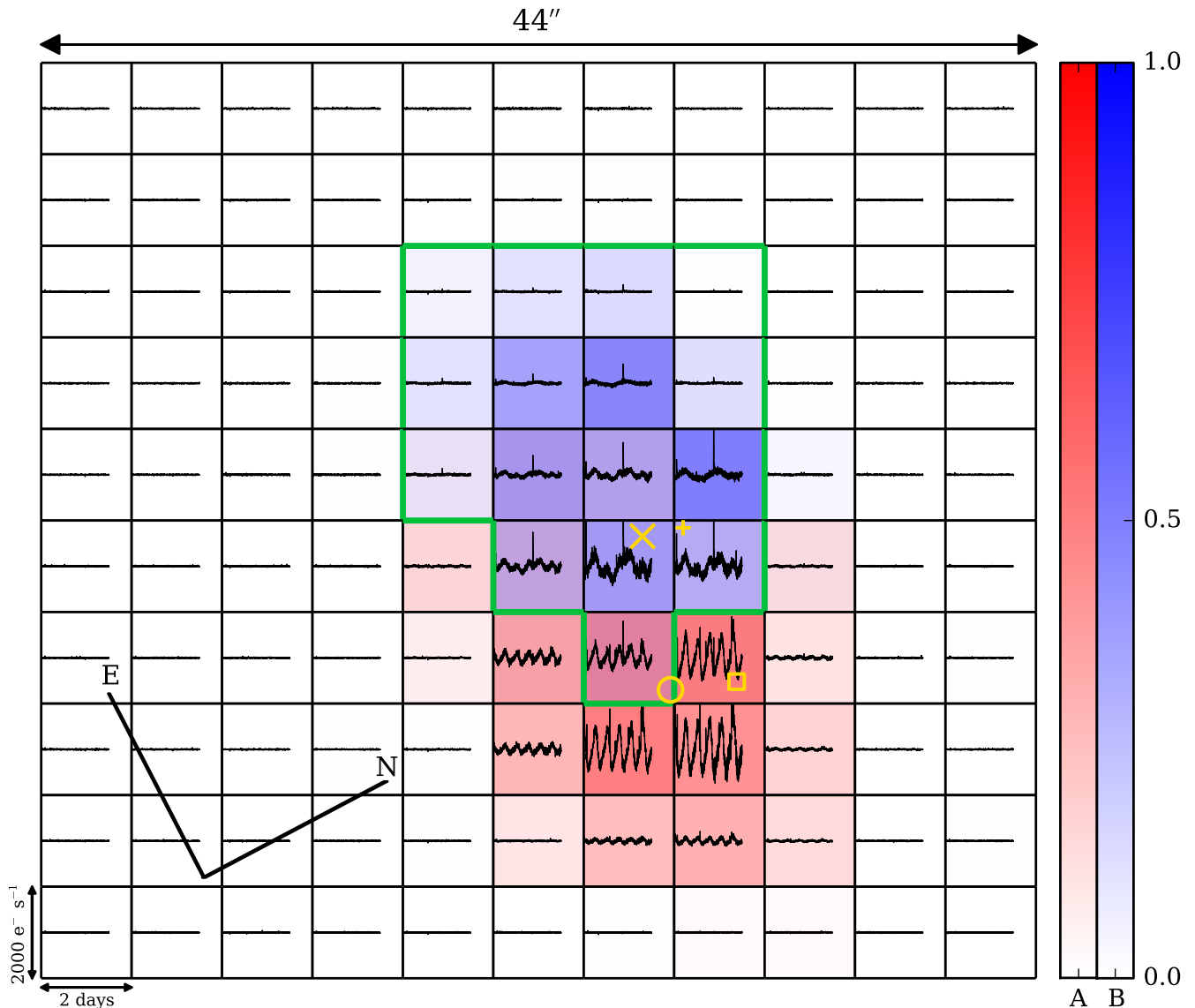


**Figure 1.** The  $11 \times 10$  grid represents the spatial extent of the target pixel mask. The field of view is shown by the  $44''$  arrow at the top, and the on-sky orientation of the mask is shown by the arrows labeled “E” and “N”. Within each cell, the pixel-level light curve is plotted. The y-axis range in each pixel is  $2000 \text{ e}^- \text{ s}^{-1}$ , and the timespan is 2 days, as denoted in the lower left corner. The color of each pixel corresponds to the strength of the starspot signals in each pixel, indicated by the color bars on the right. The locations of the PRF model sources for the A and B components are shown as a yellow circle and X, respectively. The expected positions of the stars based on their R.A. and decl. are plotted as a yellow open square and plus symbol, respectively.

indicate this is not the case for the short cadence data used for the flare analysis in §4.

The majority of the remaining flagged exposures were taken during events that have the potential to degrade the photometric precision, such as thermal equilibration after a spacecraft Earth pointing, or scattered light falling onto the mask. These flagged exposures were generally included in the PDC-SAP reduction, and we chose to include them in our reduction as well. The model fits to the flagged exposures are consistent with the unflagged exposures, although at times they appear noisier. We concluded that the risk of degraded photometric precision is outweighed by the benefit of increased time sampling when searching for flares. The effect that this noise source (and others) have on our ability to detect low amplitude flares is discussed in §4.

We ran *kepprfphot* to generate separate light curves for

all 18 quarters of long cadence data and all 3 quarters of short cadence data taken with the B component pixel mask. The calibrated fluxes in the target pixel files are already background subtracted, so as recommended in the documentation, we did not include a background source. Nor did we include parameters for pixel scale variation and focus rotation, in keeping with the documentation’s recommendation. Conservatively, we set the convergence tolerances for the residual minimization to  $10^{-7}$ . Smaller values correspond to a smaller error tolerance. We saw no change in the model output below  $10^{-6}$ , so further decreasing the tolerance would not have changed the results. The separated light curves produced by *kepprfphot* represent the source fluxes from the best-fit models to each exposure. With the separated light curves, we are able to analyze the flare and starspot properties of each star individually. However before proceeding to do so,

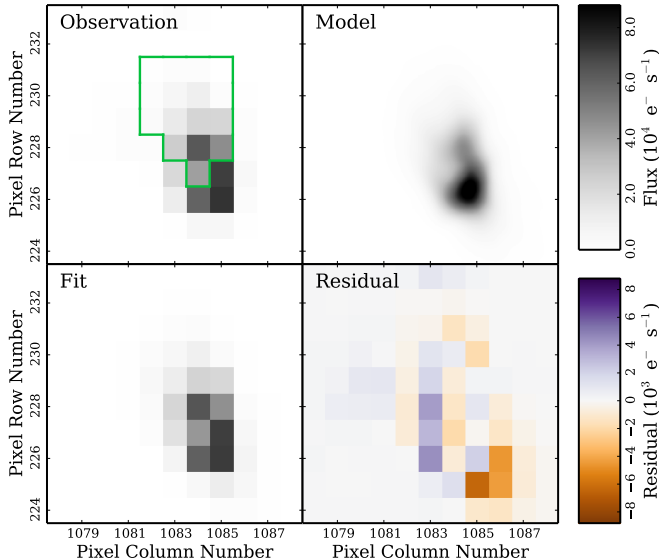


**Figure 2.** The top left panel corresponds to a single observation of the target pixel mask, with the flux in each pixel indicated by the greyscale colorbar. The green border demarcates the PDC-SAP aperture. The PyKE PRF model is in the top right panel, which is summed within each pixel to produce the fit in the lower left panel. The lower right panel shows the residual between the observation and fit. Note that the residual color bar has both negative and positive values, and has a factor of 10 smaller range than the other panels.

we next validate our model light curves to ensure that we have correctly deconvolved the two components.

### 2.3. Model Validation

To validate our PRF models, we compare our results to several well-constrained astrophysical properties of the GJ 1245 system. These include the on-sky location and angular separation of the stars, their rotation periods, and their flux ratio.

#### 2.3.1. Astrometry

The positions of the A and B components in the model for Quarter 8 are plotted in Figure 1 as a yellow circle and X, respectively. These positions correlate well with the strength of the starspot signals shown by the red and blue color bars. The expected R.A. and decl. of the A and B components have been transformed into detector coordinates using the WCS data contained in the pixel file header, and are plotted in Figure 1 as a yellow plus and unfilled square, respectively. The predicted locations agree well with the models, and differ by less than a pixel, below the level at which the model convergence is dependent. The small discrepancy could be due to a combination of uncertainties in spacecraft pointing, the WCS transformations, the 2MASS coordinates and proper motions used to calculate the R.A. and decl., as well as uncertainties in the PRF model.

Computing the angular separation of components A and B as function of time over the four years of observations provides both a means to verify our models, and a test of Kepler’s astrometric capabilities. The mean angular separation during the four years is  $6.7 \pm 0.2$ , consistent with the value of  $6''.96$  in Dieterich et al. (2012). We find that the measured separation can vary significantly within a quarter, by up to a few tenths of an

arcsecond. These intra-quarter variations repeat on an annual cycle, likely due to the stars being on different parts of the focal plane as the spacecraft executed four seasonal rolls to keep its solar panels pointed towards the Sun. This suggests that the intra-quarter variations are due to systematic effects within the spacecraft optics and detector, such as differential velocity aberration or intra-pixel sensitivity variations (Christiansen et al. 2013). It is also possible that the true PRF evolved as a function of time, and therefore differed from the model derived during commissioning. The PyKE PRF models can include parameters for pixel scale changes and PRF rotation in the fit. A test reduction including these parameters did not improve the fit and caused no change in the separation trends. The PyKE documentation does not recommend including these parameters, and we did not include them in our reductions.

In addition the intra-quarter variations, we observe a long term trend of decreasing separation between components A and B, indicative of a shift in the AC photocenter caused by the unseen C component. Plotted in Figure 3 is the angular separation of components A and B in each quarter of Kepler data, as determined by our PRF models. The vertical lines represent the range of values within each quarter due to the intra-quarter variations discussed above. Data points have been color-coded based on the observing season, i.e., spacecraft orientation, in which they were taken. Quarter 0 was a commissioning period that does not correspond to the seasons of the other quarters, so it is plotted in black. In unresolved images like the Kepler observations, a binary orbit such as GJ 1245AC would be observed as the photocenter of the two stars orbiting their center of mass. Harrington (1990) measured a photocentric perturbation for GJ 1245AC of  $0''.28$  with a period of 15.2 years. Given its expected amplitude and period, it should be detectable in the Kepler data.

Modeling the expected angular separation as a function of time requires knowing both accurate orbital parameters of the AC system, and a recent measurement of the separation between the AC and B components. The HST Fine Guidance Sensor (FGS) observations of GJ 1245 A and C described in Henry et al. (1999) were made as part of a long term astrometric program, and have yielded updated orbital parameters (Benedict et al. in prep.). The NOAO Science Archive contains a 2011 V filter observation of GJ 1245 taken with the WIYN 0.9m mosaic imager. We determined the angular separation of the AC and B components in this image by measuring the centroids with the IRAF *imexam* tool, and then converting their detector positions to R.A. and decl. using WCS transformations. The resulting angular separation is  $6''.6$  at position angle (PA) 77 degrees east of north. For comparison, the separation was  $6''.96$  at PA 83 degrees in 1998 (Dieterich et al. 2012), and  $7''.97$  at PA 98 degrees in 1975 (Harrington 1990), evidence of the several hundred year orbital motion of the AC and B components around their center of mass.

Using the AC orbital parameters derived from the FGS observations, along with the AC to B component separation measured in the 2011 ground-based image, we model the expected angular separation in Figure 3. The model is constrained so that it must pass through the ground-based data point. The slope and amplitude of the model

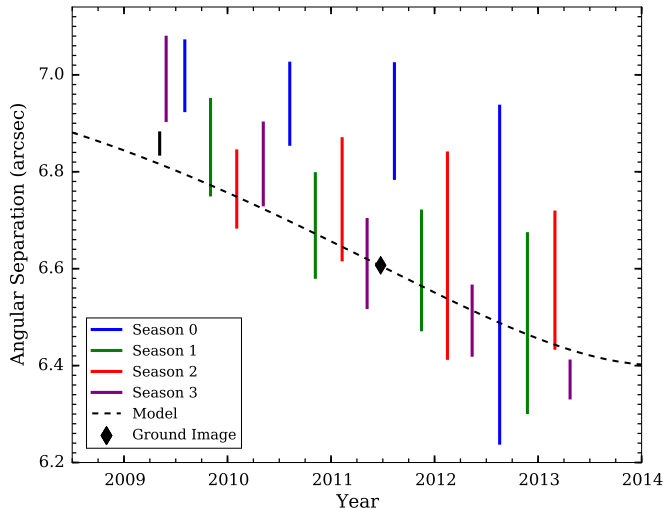


**Figure 3.** The ranges of angular separation in each Kepler quarter are plotted as vertical lines. Quarters are color-coded based on the observing season (spacecraft orientation) during which they were taken. The dashed line corresponds to the expected angular separation based on orbital parameters derived from HST FGS observations. The model is constrained to pass through the ground-based data point, shown as a black diamond. Quarter 0 does not correspond to the seasonal cycle, and is plotted in black. Quarter 17 (rightmost purple line) is only 30 days long, and therefore has a smaller variation.

is consistent with the observations. The Season 0 data points have the largest scatter, and if they are disregarded the model agrees well with the data, given the fairly large intra-quarter variations. We did not attempt to correct for these variations, so a more detailed analysis and comparison to the much more precise HST observations is beyond the scope of this paper. However, these results serve to validate our PRF models, given their agreement with the contemporaneous ground-based image, and that the long term trend is consistent with an astrometric perturbation due to the C component.

### 2.3.2. Rotation Periods

An example of the short cadence separated light curves produced by *kepprfphot* is shown in Figure 4. By eye, it is easy to see the two starspot signals, as well as flares that occur on one component but not the other. Lomb-Scargle periodograms of the 4 year, detrended, long cadence light curves discussed in §3 are shown in Figure 5. In the A component periodogram, there is a large peak at the 0.26 day rotation period of the A component, as well as at  $1/2$  of the A period. In the B component periodogram, there is a large peak at the 0.71 day rotation period of the B component, and at  $1/2$  of the B rotation period. There is also a small peak at the A component period. These periodograms indicate that the PRF models have cleanly deconvolved the two components with minimal cross-contamination.

### 2.3.3. Flux Ratios

The PRF models consistently converge to a flux for the A component that is on average 2.9 times that of component B, and varies between quarters from 2.5 to 3.3. From the published photometry, the flux ratio of the A component to the B component is 1.84, 1.74, 1.64, and 1.57 at *B* (Dahn et al. 1976), *V*, *R*, and *I* (Reid et al.

2004), covering the entire Kepler bandpass. Here we neglect the small flux contribution from the C component, as it is  $\sim 94\%$  less bright than the A component. In the 2011 ground-based *V* filter image, the flux ratio is 1.8. The A and B components in their PDC-SAP light curves have a mean flux ratio of 2.0 over the four years of observations. While the A component PDC-SAP light curve appears to be uncontaminated, there is some A component contamination in the B component PDC-SAP light curve. Removing this contamination would raise the flux ratio somewhat higher than 2.0, in closer agreement with our models, but further from the ground-based data. The discrepancy between the PRF model and the ground-based photometry does not affect our results, other than to offset the flare energy distributions (see §4), but we discuss it here for completeness.

If the discrepant flux ratio were due to a systematic misassignment of flux by the model, it should appear in the model residuals. The residuals in the lower right panel of Figure 2 are typical of those for the model fits over the four years of data. Note that the residuals can have both negative and positive values, as the model can overpredict or underpredict the flux in a pixel. While the residuals for an individual pixel are as large as a few thousand  $e^- s^{-1}$ , this represents  $\lesssim 1\%$  of the total flux in the pixel mask of approximately  $500,000 e^- s^{-1}$ .

Furthermore, the residuals show no spatial correlation, in the sense that the model does not systematically assign more flux to one component at the expense of the other. We verified this for each quarter of data by examining the 15 nearest pixels to the A and B component source locations. If a pixel was close to both components, it was assigned to the nearest component. For these two regions of pixels that “belong” to each component, we calculated the residuals between the observation and the model. The sum of the residuals across each region was relatively small, between a few hundred to a few thousand  $e^- s^{-1}$ . This is not large enough to explain the unexpectedly large flux ratio consistently obtained by the model fit. It appears that the PRF model is accurately reproducing the true PRF, and that the PRF itself is causing the B component to appear fainter relative to the A component than it is in ground-based images.

Potential sources of error in the PRF model listed in Bryson et al. (2010) are changes in focus since the commissioning observations, blends or variability in the stars used to compute the model, CCD non-uniformities, and the PRF dependence on star color, which was not modeled. The dithering observations of a finite number of calibration stars did not sample every pixel on the detector, so the PRF model must interpolate to be defined over the entire detector, limiting its accuracy. These and other factors may contribute to the residuals in the models, as well as the intra-quarter variations in angular separation.

While the residuals within a given pixel can be relatively large, the sum of the residuals across the mask remains small, of the order a few hundred  $e^- s^{-1}$ . This means that the model is recovering all of the flux in the mask, although in some cases it may be assigning some flux to the wrong component. Despite the discrepant flux ratios we obtain, the latter scenario appears unlikely, given the lack of starspot signal contamination in the A and B component light curves. While it is possible that



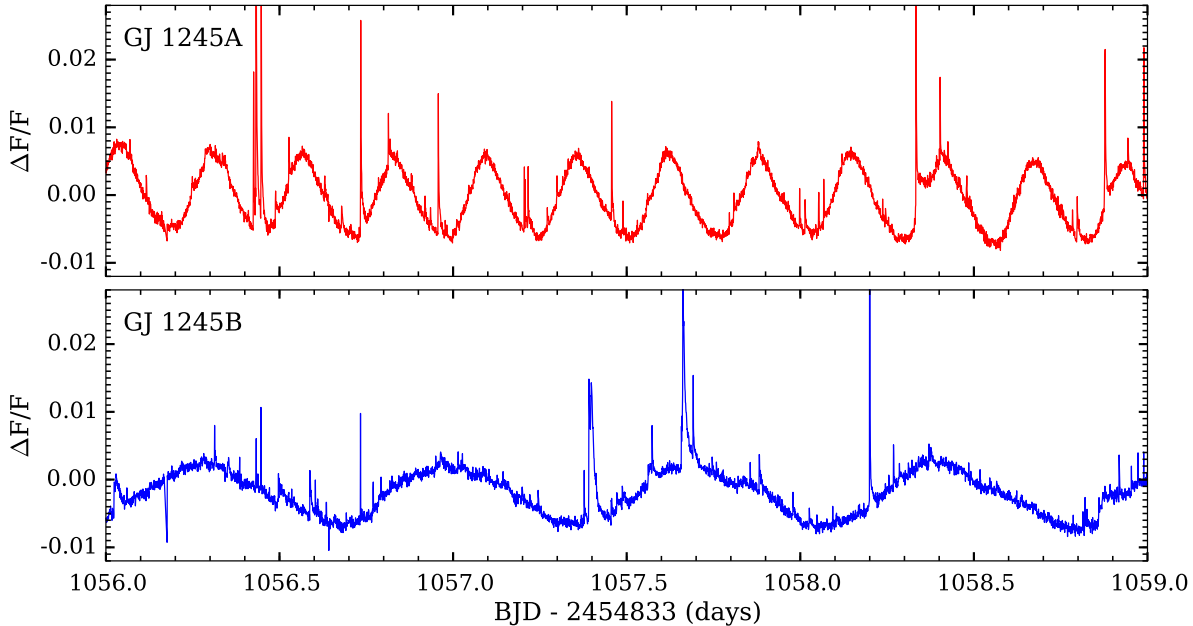


**Figure 4.** An example of the separated, short cadence light curves generated by the *kepprfphot* routine, in terms of relative flux. Nearly all of the flares shown are separate events occurring on only one star. The negative flux excursions are single-exposure errors in the models.

our residuals and the flux ratio could be improved by additional modeling, the PyKE routines and the PRF model were developed by the Kepler science team, and we did not endeavor to augment them. Based on the overall strong agreement with the astrophysical constraints outlined above, we believe our light curves represent the best-fit models, and can reliably be used for the analysis that follows.

### 3. STARSPOT EVOLUTION

We used the separated, long cadence light curves to analyze the starspot evolution of each star, as the 30 minute cadence sufficiently samples the 8 and 17 hour period starspot modulations. In this section we describe how long-term trends were removed from the light curves, and examine the evolution of the starspot features.

#### 3.1. Light Curve De-trending

The separated light curves exhibit smooth, long-term trends that are typical of uncalibrated Kepler data. M dwarfs have been observed to exhibit long-term *VRI* photometric variability of up to 5% on multi-year timescales (Hosey et al. 2014). Such variations could in principle be detectable in our data. Unfortunately, because Kepler was not designed for absolute photometry, we are unable to determine whether the observed long term trends are physical or due to instrument systematics. Because our starspot analysis is concerned with short-term changes in the relative brightness of each star, we simply removed these long term trends and normalized the light curve into units of relative flux as described below.

We first smoothed the light curve using the one-dimensional Gaussian filter in the Python SciPy package, in order to trace the low frequency trends in the light curves without affecting the higher frequency starspot signals. A Gaussian filter functions as a low pass filter, and has a Gaussian frequency response function. The

standard deviation,  $\sigma$ , of the kernel determines the cutoff frequency of the filter. Increasing  $\sigma$  decreases the cutoff frequency. In addition to long-term trends, the light curves also have some discontinuities that occur at gaps in data. We addressed this by identifying all data gaps longer than 0.5 days, and smoothing each section of light curve separately. There remained a few discontinuities that did not occur at data gaps, which we also analyzed individually.

So that flares did not skew the de-trending, we performed a initial smoothing with a kernel size of  $10\sigma$ , and then rejected all points on the original light curve that were more than two standard deviations away from the smoothed light curve. We then smoothed the original light curve, with flares removed, using a kernel size of  $40\sigma$ . We chose this kernel size because a Gaussian filtering of evenly spaced data at a 30 minute cadence with a  $40\sigma$  kernel completely attenuates all signals below 1 day. The resulting smoothed light curve does not contain the starspot modulations, but traces the long term trends in the original light curve. The final, de-trended light curve was produced by subtracting the smoothed light curve from the original light curve, and then dividing by the median flux value of the entire un-smoothed four year light curve. The de-trended light curve has units of relative flux, or

$$\frac{\Delta F}{F} = \frac{f - f_s}{f_0} \quad (1)$$

where  $f$  is the flux in the original light curve,  $f_s$  is the flux in the smoothed light curve, and  $f_0$  is the median value of  $f$  over the four year dataset. We stress that the purpose of this de-trending is to trace the low frequency trends and convert the light curve to units of relative flux. The size of the Gaussian kernel was chosen so that the de-trending did not affect the short period starspot signals.

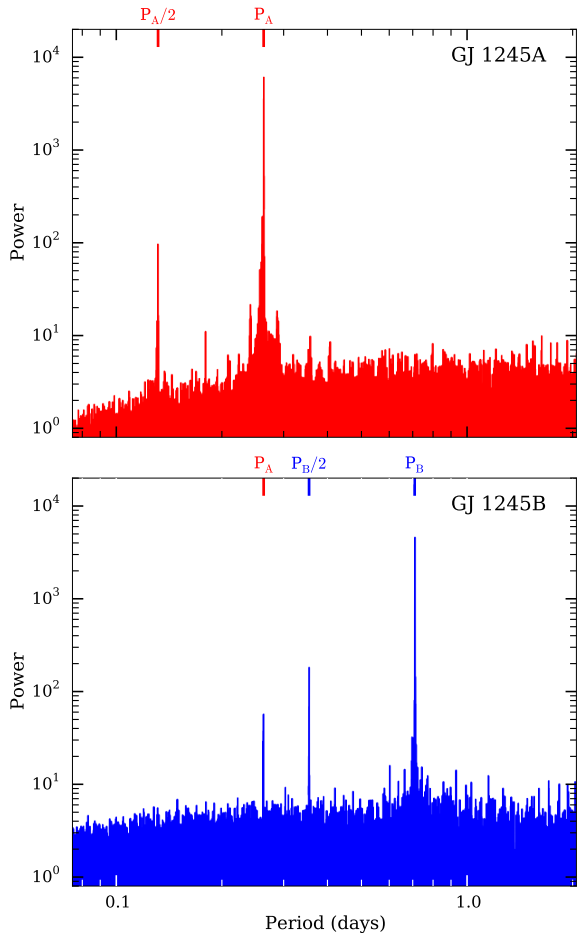


**Figure 5.** Lomb-Scargle periodograms for the four year, long cadence, separated light curves. The light curves were de-trended and converted to units of relative flux prior to generating the periodograms. Peaks corresponding to the full and half rotation periods of stars A and B are labeled. The other small peaks in the A component light curve do not correspond to the rotation period of either star, and are likely due to noise.

### 3.2. Differential Rotation

Because the light curves represent the integrated flux from the hemisphere of the star visible at a given time as the star rotates, we are limited in our ability to determine the spatial distribution of the spot regions. For instance, we cannot say whether there are a few large spots or many small spots distributed over the star. We therefore refer to the light curve modulations as dark and light “features”, with the minimum in the modulation corresponding to the visible hemisphere of the star that has the largest amount of spot coverage.

However, there are some basic measures of the starspot evolution that can be obtained from the light curves. Figure 6 shows the relative amplitudes of the starspot modulations as a function of time, with the light curves averaged in 10 day bins. The A component modulation generally has a larger relative amplitude, but the modulations on both stars show significant variations in amplitude over time. As a check of our models, we performed the same de-trending procedure on the long cadence PDC-SAP light curve for the A component, and the relative amplitude evolution appears nearly identical to that from our A component model light curve in Fig-

ure 6. The changes in starspot modulation amplitude are consistent with the spectropolarimetric results of Morin et al. (2010), who saw changes in the large scale magnetic field on GJ 1245B during a three year observing campaign.

Another measure of the starspot evolution is to examine if there is any phase shift in the starspot modulation. We assume that the modulations are due to darker spot regions rotating into and out of view, changing the integrated flux from the visible hemisphere of the star. Thus the starspot modulation as a function of rotation phase gives an indication of how the spots are distributed longitudinally on the star. In Figure 7, the light curves have been phase-folded at the respective rotation period of each star, and then averaged in 10 day bins. The light curves have been folded over two phases for visual clarity. A more detailed description of this phase-folding procedure and its application to modeling starspot features will be given in a forthcoming paper (Davenport et al. in prep). We fit the starspot features with bivariate Gaussians, where the x and y-dimensions are time and phase, and the z-dimension is relative flux. A cut through a bivariate Gaussian along the x-y plane creates an ellipse. In Figure 7, we cut through each Gaussian at its  $2\sigma$  value, and represent the time axes of the resulting ellipses as yellow lines. The purpose of these fits is to guide the eye, and to enable a quantitative discussion of the spot evolution.

These stars are remarkable for the long-lived nature of their spot features. On the A component, we fit two spot features, both of which remain at nearly constant phase. This could also be interpreted as a single, long-lived spot. On the B component, we fit three spot features, all of which show a more rapid phase evolution than the features on the A component. Most notably, there is a dark feature migrating from phase  $\sim 0.5$  to  $\sim 0.0$  between days  $\sim 350$  and  $\sim 700$ . This feature coincides with the minimum in the relative amplitude seen in Figure 6, indicating that the spot coverage was temporarily more evenly distributed with longitude. As is the case for the entire light curve, there is almost no signal present from the A component in this section of the B component light curve. This rules out the migrating feature being caused by contamination from the A component.

The phase evolution of these features can be explained by differential rotation. For example, a spot near the pole and a spot near the equator would appear to shift in phase relative to each other if there is a variation in rotation rate with latitude. The features in Figure 7 could potentially be due instead to the meridional flow of spots, or the emergence and disappearance of spots. However for component B, the former effect is too slow to explain the rapid phase evolution, and the latter is unlikely to result in the coherent phase evolution that is observed. The rate of change of phase with time,  $\Delta\Omega$ , reported in Table 2, gives a lower limit on the difference in rotation rate between the equator and the pole. Differential rotation also affects the measured period of the starspot modulation if spots are present at different latitudes. This creates some uncertainty in the rotation period determination. Analyzing each of the 9 sub-quarters ( $\sim 1$  month in duration) of short cadence separated light curves individually, we find mean rotation periods of  $0.2632 \pm 0.0001$  and  $0.709 \pm 0.001$  days for the A and B components, respectively.



While the exact period determined depends on the subset of data analyzed and its duration, we confirm the rotation periods reported in Paper 1 within the uncertainties quoted above.

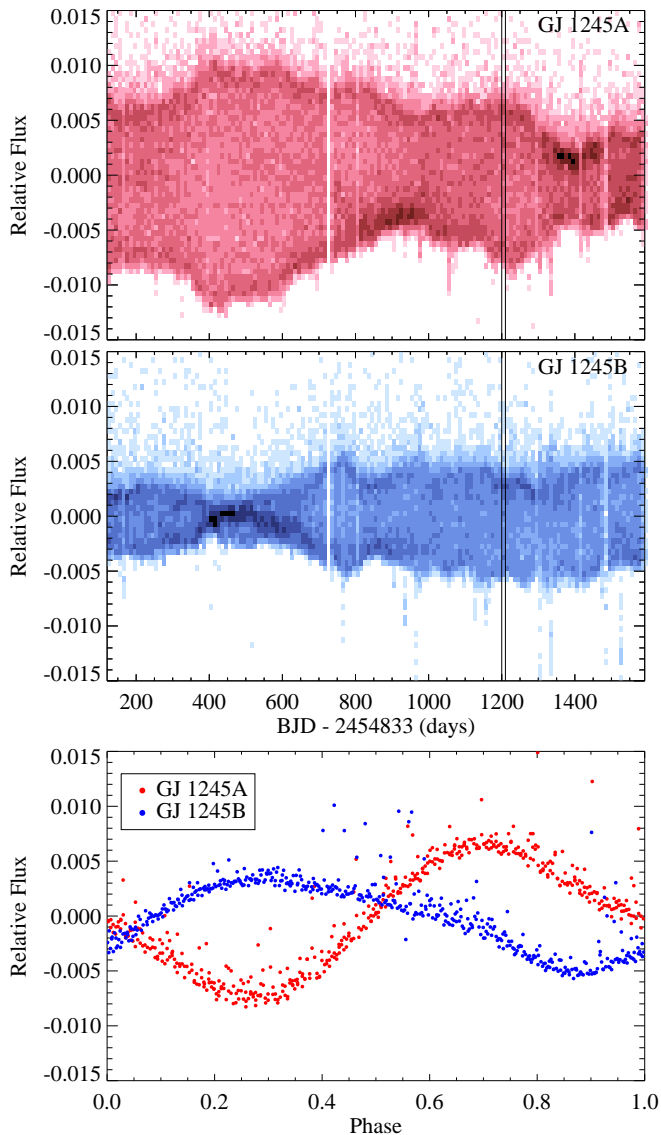


**Figure 6.** The top two panels show the relative amplitudes of the starspot modulations versus time, with the light curves averaged in 10 day bins. In the bottom panel, phase-folded light curves are plotted for the bins represented by the vertical lines in the top two panels. The contours in the top two panels correspond to the density of points in the bottom panel. Note how the amplitude of the light curves in the bottom panel corresponds to the amplitude of the contours in the top two panels. Flares are shown as positive flux excursions, while the negative excursions are due to small errors in the detrending discussed in §3.

#### 4. FLARES

The 1 minute sampling of the short cadence data is most sensitive to flares. Although some flares are evident in the long cadence data, we have found that the 30 minute sampling makes it difficult to directly compare the measured energies to the short cadence data. There-

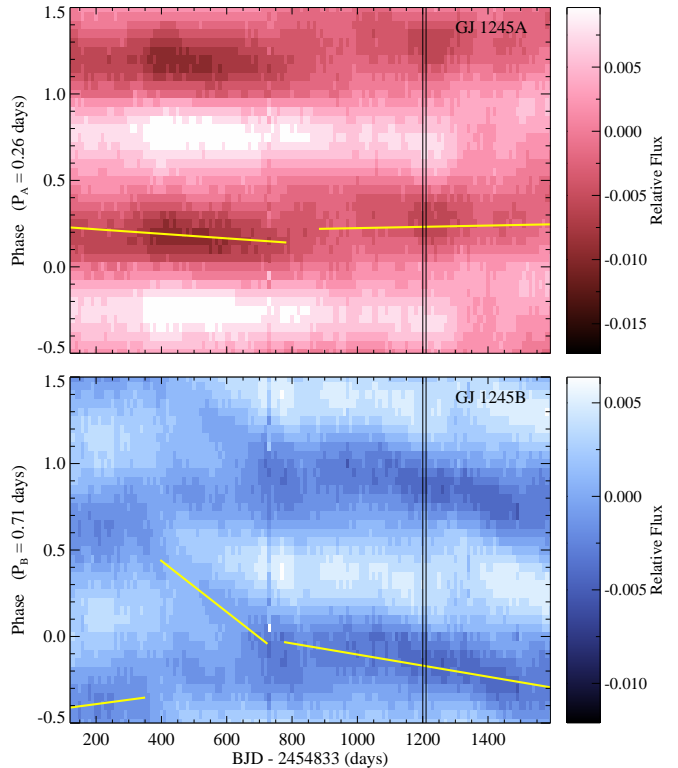


**Figure 7.** Starspot modulation phase versus time. The light curves have been folded over two phases at the respective rotation period of each star, and averaged in 10 day bins. In this figure, the contours represent relative flux. For the bins represented by the vertical black lines, note how the darkest contours correspond to the minima in the phase-folded light curves in the bottom of panel of Figure 6, at phase 0.3 and 0.9 for components A and B, respectively. We fit the spot features with bivariate Gaussians. Yellow lines represent the  $2\sigma$  values along the time axis of the Gaussians.

fore we limit our flare analysis to the separated short cadence light curves, which comprise 3 quarters of Kepler monitoring. In this section, we describe how flares were identified in the light curves, and how the flare samples were prepared. We next discuss the effects of non-linear CCD response for high energy flares. Finally, we determine flare rates for each star, characterize their power law distributions, and determine the fraction of the stars' total energy emitted in flares.

##### 4.1. Flare Identification

We identified flares using the automated selection procedure described in §2.1 of Paper 2. Briefly, the light curves were first iteratively smoothed to remove the periodic starspot modulations. This step is necessary because many flares have amplitudes smaller than the starspot modulation, and therefore would not be identified by a simple threshold search of the unmodified light curve. We note that this is a different smoothing procedure than the one described in §3. Here the function is to remove the starspot signal but preserve the flares. Flare candidates were identified as two or more consecutive observations with positive flux excursions more than 2.5 times the standard deviation of the smoothed light curve. The light curves with the tagged flare candidates were visually inspected to ensure that the selection procedure did not mistakenly identify data gaps or discon-

tinuities as flares. Instances where this occurred were removed from the sample.

Due to noise in the light curves, there is a minimum flare energy below which we cannot reliably identify flares. Here we determine the energy of a flare in terms of its equivalent duration, i.e., the area under the flare light curve, measured in relative flux units. The calculation of equivalent duration is discussed in greater detail in Hunt-Walker et al. (2012). Equivalent duration has units of time, but is not to be confused with the duration of time over which the flare occurred. Multiplying the equivalent duration by the quiescent luminosity of the star gives the flare energy.

For a flare of a given equivalent duration,  $\mathcal{E}$ , and duration,  $\tau$ , in time, we define the signal-to-noise (S/N) of the flare as

$$S/N = \frac{\mathcal{E}}{\sqrt{\mathcal{E} + \sigma\tau}} \quad (2)$$

where  $\sigma$  is the standard deviation of the “continuum” light curve around the flare. Each flare candidate was visually inspected, in descending order of S/N. For both stars, spurious flare events began to contaminate the sample at a S/N value of 1.4. We therefore excluded flare candidates below this threshold. The S/N of flares correlates with equivalent duration, and therefore energy. Although a S/N value of 1.4 corresponds to the same equivalent duration value of 2.3 seconds for both stars, it corresponds to a lower flare energy limit on the B component, because a lower energy flare is easier to detect above the quiescent flux of the intrinsically fainter B component. Although many of the flare candidates below the threshold are real flare events, we set the threshold conservatively high to limit the impact of systematic effects in the model light curves.

As determined in §2.3 of Paper 1, the total quiescent luminosity of the GJ 1245 system in the Kepler bandpass is  $\log L_{Kp} = 30.22 \text{ erg s}^{-1}$ . The quiescent luminosity was determined using the apparent Kepler magnitude of the GJ 1245 system listed in the Kepler Input Catalog, the zero-point of the Kepler magnitude system, and the trigonometric distance of the system. The individual quiescent luminosities of components A and B can be found from the total system luminosity if the flux ratio of the two stars in the Kepler bandpass is known, neglecting the small flux contribution of the C component. We adopt the flux ratio of 1.64 in the  $R$  filter based on the values in Reid et al. (2004). Among the standard photometric filters, the  $R$  filter is most representative of the Kepler wavelength response. This yields individual quiescent luminosities of  $\log L_{Kp} = 30.01$  and  $29.80 \text{ erg s}^{-1}$  for the A and B components, respectively. We note that this adopted flux ratio is significantly smaller than that of our PRF models. Given the uncertainties associated with the Kepler PRF, we prefer the well calibrated optical photometry. We assume that the discrepant PRF model flux ratio is the result of the spacecraft optics and detector, that changes in brightness due to starspots and flares are proportional to the baseline, quiescent brightness. Thus this does not affect the measured relative flare energies, i.e, the equivalent durations.

Because the light curves were produced by fitting a PRF model to the pixel-level data, it is possible that a flare event, particularly one with a large amplitude,

could appear in the pixels of both stars and be included in both light curves despite having originated from only one component. In this case, the flares in each light curve should reach their peak fluxes at the same time, and have similar light curve morphologies. Approximately 4% of the flares in the sample for each star had peak times that differed by less than 3 minutes from a flare on the other star above a S/N of 1.4. The remaining 96% were considered as separate events. Given the 1 minute time sampling of the short cadence data, two events occurring more than 3 minutes apart should easily be resolved.

The 4% of flares that overlapped by less than 3 minutes were discarded from the samples for both stars, with the exception of a few flares for which the equivalent duration was a factor of 10 greater on one star than the overlapping flare on the other star. In these cases, we were confident as to which component the flare originated from, and kept the larger equivalent duration flare while discarding the smaller. The overlapping flares present several issues for the flare samples. The A component is brighter, so a flare from component A is more likely to contaminate component B than vice versa. However, as they only represent 4% percent of the flares, this does not significantly bias the sample. It is possible that some of the discarded overlapping flares are in fact two separate events that happened to occur on each star at nearly the same time. The likelihood of such events is rare, and because flares occur randomly in time this should not affect the relative occurrence rates for each star.

We have neglected the contribution of the C component to the flare sample for the A component. While the C component may flare often, nearly all of its flares would be undetectable in the Kepler data. For a flare on the C component to be visible in the Kepler data, it must be brighter than the quiescent flux of the A component. This would require a flux enhancement of over 3 magnitudes. The flare frequency distributions (FFDs) of Hilton (2011) put an upper limit on the occurrence of such flares on M6 – M8 stars at approximately once per 100 hours. This is a conservative upper limit on the occurrence rate, as the flare sample was based largely on M6 and M7 stars, so the occurrence rate of such large flares would be lower for an M8 analog to GJ 1245C. During the 5,491 hours of Kepler short cadence exposures of the GJ 1245 system, we would expect to detect no more than 55 flares from the C component. However, such a flare would only remain at its peak, detectable brightness for a short time. They would appear as short-lived, low energy flares in the A component light curve, and would have been discarded by the minimum signal to noise threshold applied to the sample.

#### 4.2. CCD Non-linearity and Saturation

Upon investigation of the target pixel files, we found that some high energy flares caused the Kepler CCD to respond non-linearly, and in some cases saturate. The effect on our flare samples is discussed in §4.3, but we first provide some details of our analysis, as they are relevant to other investigations of impulsive phenomena in the Kepler dataset. We examined the raw counts in the short cadence target pixel files, focusing on the brightest pixels for each component, as they are the most likely to respond non-linearly during a flare. It was crucial to inspect the uncalibrated raw counts, because the cali-

**Table 1**  
Flare Statistics

Star	# Flares	Flares per day	Range $\log E_{Kp}$ (erg)
GJ 1245A	683	3.0	30.38 - 32.63*
GJ 1245B	605	2.6	30.16 - 33.14*

\* This sample is comprised of all flares that met the sample criteria described in §4.1, including those affected by CCD non-linearity. The upper energy ranges are therefore lower limits.

brated fluxes can disguise the effects of non-linearity and saturation. During Quarters 8, 10, and 11, the median counts in the brightest pixel for the A component were 46%, 83%, and 50% of the full well depth (10093 ADU; Van Cleve et al. 2009). The corresponding values for the B component were 37%, 45%, and 45%. Because the stars changed locations in the focal plane between spacecraft rolls, roughly half of the flux from the A component was concentrated in a single pixel during Quarter 10. In Quarters 8 and 11, the flux was distributed more evenly across several pixels, as was the flux from the B component during all three quarters. As the quiescent counts in these pixels are already a significant fraction of the full well depth, a flare that temporarily increases the counts in a pixel by more than a factor of two or three is a cause for concern.

The classical flare temporal morphology discussed in § 2.2 of Paper 1 is characterized by a rapid rise in flux, followed by a rapid decay, and then a slower exponential decay. A short cadence observation represents the sum of nine 6 second exposures (Van Cleve et al. 2009). Given the rapid rise and decay of a typical flare, a pixel could reach its full well depth in one or more these exposures even if the mean counts for all nine exposures is less than the full well depth. In this case the fluxes measured for the flare would only be lower limits. Because the CCD responded non-linearly, and because no information is retained on the individual 6 second exposures, we are unable to quantify the extent of the energy underestimation.

Although up to 25% and 9% of the flares in the sample for components A and B, respectively, may have caused the detector to respond non-linearly and potentially saturate, it does not appear that this caused any significant CCD bleeding effects onto adjacent pixels, with one notable exception. For the largest amplitude flare in the observations, bleeding along two pixel columns is evident, and at least 13 pixels are saturated during the brightest point in the flare. Additional bleeding likely occurred in pixels outside of the target pixel mask. The flare appears in the separated light curves of both stars, and was discarded from the sample under the criteria described previously.

#### 4.3. Flare Rates and Statistics

The statistics of the flare samples are summarized in Table 1, and the flare energies are plotted as a histogram in Figure 8. This sample is comprised of all flares that met the sample criteria described in §4.1, including those affected by CCD non-linearity. The sharp turnover at

lower energies is the result of the signal to noise cutoff in the flare samples. We note that by virtue of being on the same pixel masks, the two stars were observed for the same amount of time, so their flare distributions can be compared without normalization. The energy distribution histograms are similar, but are offset in energy due to the different quiescent luminosities of the two stars. For flares above the S/N threshold, the average rates are also similar, with the A component exhibiting 3.0 flares per day, compared to 2.6 on the B component. These similarities are somewhat unexpected if activity correlates with rotation period, given that the A component rotates almost three times faster than B.

The cumulative FFDs for components A and B are shown in Figure 9. The FFD gives the cumulative number of flares greater than or equal to the given energy that occur each day. Flare frequency is plotted versus energy on the top panel of Figure 9, and versus equivalent duration in the bottom panel. While it is useful to present the FFD in physical units, this is not a fair representation of the relative activity of the two stars. In the top panel, most of the offset between the two FFDs is due to the quiescent luminosity difference of the stars. In terms of equivalent duration, the FFDs lie closer together. The equivalent duration distribution represents the energy released in flares relative to the total energy output of the star (see Eqn. 6 below).

Flare occurrence is typically modeled using a power law distribution in energy of the form

$$N(E)dE = \beta E^{-\alpha} dE \quad (3)$$

where  $\beta$  is a constant. The slope of the cumulative FFD is equal to  $1 - \alpha$ . As seen in the bottom panel of Figure 9, the FFDs for both stars are not fit by single power laws, shown as green lines. This is due to the non-linear response of the CCD to high energy flares (see §4.2). Because the equivalent duration (and energy) measurements for these flares are only lower limits, we underestimate the frequency of high energy flares, causing the FFD to artificially steepen at high energies. The A component FFD begins to deviate from a single power law at an equivalent duration of approximately 10 seconds. The B component FFD is well fit by a single power law up to an equivalent duration of approximately 25 seconds. As expected, the deviation from a single power law is more pronounced for the A component. Due to its greater apparent brightness, a lower energy flare on the A component will cause its corresponding pixels to respond non-linearly compared to the fainter B component. Due to the non-linear response of the CCD, we are unable to determine if there is any intrinsic change in the power law slope at higher energies.

The measured energies for the high energy flares in our sample are compromised due to non-linear CCD response, and they are not included in the power law fits. Some turnover is evident in the FFDs below an equivalent duration of 2.7 seconds, due to incomplete detection of the lowest energy flares. We therefore fit power laws to the FFDs over an equivalent duration range of 2.7 – 10.0 seconds for each star. We assume that the samples are complete in this range, that these flares did not cause the detector to respond non-linearly, and that their energies are well constrained. The uncertainty in the number of observed flares at a given equivalent dura-

tion was assumed to follow a Poisson distribution. The largest contribution of uncertainty in the equivalent duration measurements is due to fitting of the underlying starspot modulation. This sets the baseline flux against which the flare is measured. We found that changes in the size of the window of quiescent light curve around the flare that is fit can change the measured equivalent duration by up to 10%. In most cases, the change was less than a few percent, but we conservatively set the uncertainties on all measured equivalent durations at 10%.

The power law fit was performed using a Bayesian Markov chain Monte Carlo-based algorithm (Kelly 2007). The slopes with uncertainties are reported in Table 2. The FFDs for GJ 1245 A and B presented here supersede the combined FFD of Paper 1, which was based on the combined PDC-SAP light curve, and included flares from both stars. The power law slope for the combined FFD in Paper 1 was  $-1.32$  ( $\alpha = 2.32$ ), steeper than what we report here for the individual stars as a result of including the lower limits for the high energy flares in the power law fit.

In Figure 10, the number of flares and flare energies occurring on each star are plotted versus rotation phase. Only flares with equivalent durations less than 10 seconds are plotted, for which the energies are well constrained. For reference, one month of the nine month long separated short cadence light curves have been folded at the rotation period of the respective star. To the eye, the number distribution on the A component is suggestive of a correlation with rotation phase. However, any potential phase dependence is not statistically significant, given the assumed Poisson errors. The histogram is consistent with a constant distribution at the median value of the histogram with a reduced  $\chi^2$  of 0.87. For the B component histogram, the reduced  $\chi^2$  of constant fit is 0.88. Similarly, the flare energies show no correlation with rotation phase. These results suggest that the flare-producing regions are uniformly distributed in longitude across the star.

#### 4.4. A New Metric for Comparing Flare Rates

From the power law distribution in Equation 3, an analytical relation can be obtained for the total energy,  $E_{tot}$ , released from flares with energies in the range  $E_0$  to  $E_1$ .

$$E_{tot} = \frac{\beta}{2 - \alpha} (E_1^{2-\alpha} - E_0^{2-\alpha}) \quad (4)$$

Alternatively, in terms of equivalent duration,  $\mathcal{E}$

$$\mathcal{E}_{tot} = \frac{E_{tot}}{L_{Kp}} = \frac{1}{L_{Kp}} \frac{\beta}{2 - \alpha} (\mathcal{E}_1^{2-\alpha} - \mathcal{E}_0^{2-\alpha}) \quad (5)$$

The constants for these relations are determined from the power law fit to the FFD. The total luminosity emitted in flares relative to the total luminosity through the Kepler bandpass is

$$\frac{L_{fl}}{L_{Kp}} = \frac{E_{tot}/t_{exp}}{L_{Kp}} = \frac{L_{Kp} \mathcal{E}_{tot}/t_{exp}}{L_{Kp}} = \frac{\mathcal{E}_{tot}}{t_{exp}} \quad (6)$$

where  $t_{exp}$  is the total exposure time of the observations. Note that by expressing the ratio  $L_{fl}/L_{Kp}$  in terms of equivalent duration, the Kepler luminosity cancels out, removing a source of uncertainty in comparing  $L_{fl}/L_{Kp}$  for different stars.

The values of  $L_{fl}/L_{Kp}$  for components A and B reported in Table 2 represent an integration of the power law distribution (Eqn. 5) over the equivalent duration range 2.7 – 10.0 seconds. These agree well with the values found by simply summing the equivalent durations of the observed flares over the same range. Note that in Table 2 of Paper 1,  $L_{fl}/L_{Kp}$  is reported as  $f_E$ . The values reported here supersede that of Paper 1, which was based on the unresolved light curve for components A and B, and was integrated over a wider equivalent duration range. We caution that due to the nature of power law distributions,  $L_{fl}/L_{Kp}$  depends on the range of equivalent durations (or energies) considered. Thus the limits of integration should be reported along with the values for  $L_{fl}/L_{Kp}$ , and taken into account when comparing to other stars.

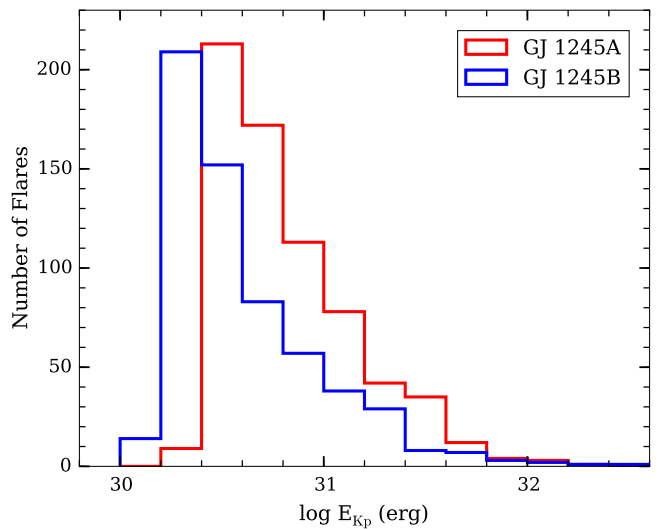


**Figure 8.** Flare energy histograms for stars A and B. The sharp cutoffs at low energy are due to the minimum signal to noise threshold assigned to the flare sample.

## 5. DISCUSSION

We have used the PyKE PRF modeling routines to produce separate light curves for two active M dwarfs, GJ 1245 A and B, which were previously unresolved in the Kepler pipeline processing. Comparison of the model output to well constrained astrophysical parameters of the system confirms that we have successfully deconvolved the two stars. The model recovers the starspot modulations and flares on each star with minimal cross-contamination. The angular separation of the two stars, as determined by the PRF models, decreased in a manner consistent with an astrometric perturbation due to the orbit of the unseen C component. Unfortunately, the 4 years of Kepler observations only cover  $\sim 25\%$  of the total orbital period, and are plagued by significant systematics. A more robust astrometric analysis lies beyond the scope of this paper. We hope that our results may encourage others to conduct a more in-depth search for astrometric perturbations in the Kepler dataset.

Because GJ 1245 A and B are coeval and have similar masses, we are able to take a holistic view of the dependence of flare occurrence and differential rotation on rotation rate. This is summarized in Table 2, in which

**Table 2**  
Comparison of Active M Dwarfs

Star	$\log L_{Kp}$ ( $\text{erg s}^{-1}$ )	$P_{rot}$ (days)	$\log L_{fl}/L_{Kp}$ *	$\alpha^\dagger$	$\Delta\Omega$ ( $\text{rad day}^{-1}$ )	$\log L_{H\alpha}/L_{bol}$
GJ 1243 <sup>+</sup>	30.67	0.5927	$-3.78 \pm 0.01$	$1.92 \pm 0.01$	0.004	-3.56
GJ 1245A	30.01	0.2632	$-3.93 \pm 0.02$	$1.99 \pm 0.02$	0.0008	-4.14
GJ 1245B	29.80	0.709	$-4.00 \pm 0.02$	$2.03 \pm 0.02$	0.009	-3.97

<sup>+</sup> The values for GJ 1243 are taken from Papers 1 and 2.

<sup>\*</sup> These values represent the integration of the energy distribution power law over the equivalent duration range 2.7 – 10 seconds.

<sup>†</sup> The slope of the cumulative FFD is  $1 - \alpha$ .

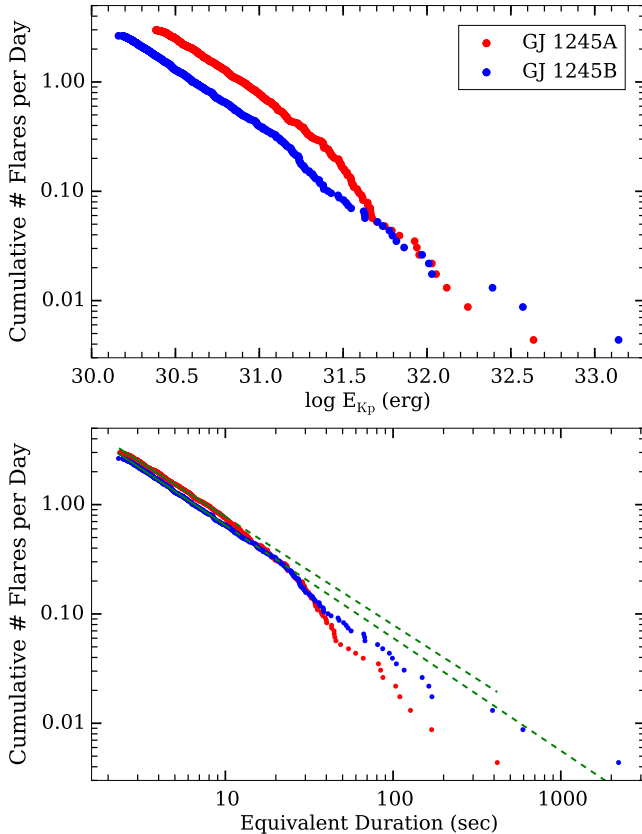


**Figure 9.** The cumulative flare frequency distributions for stars A and B are plotted versus energy (top panel) and equivalent duration (bottom panel). For a given energy (or equivalent duration) on the x-axis, the cumulative number of flares per day greater than or equal to that energy is given on the y-axis. The power law fits (solid green lines) do not include flares with  $E_{Kp} > 32.3$  (dashed green lines).

we also include results for the active M4 star GJ 1243. Although we do not know the age of GJ 1243 relative to the GJ 1245 system, it is a useful comparison star that has been studied in a similar manner using Kepler data. The rotation period for GJ 1243 is taken from Paper 1, while the flare sample is taken from Paper 2. For consistency, the flare energy distribution slope,  $\alpha$ , and the value for  $L_{fl}/L_{Kp}$  for GJ 1243 were determined using the same criteria described in §4 for GJ 1245 A and B. The measure of differential rotation,  $\Delta\Omega$ , corresponds to the value for the fastest migrating spot feature on each star. It represents a lower limit on the shear between the equator and the poles, expressed in radians per day. Dif-

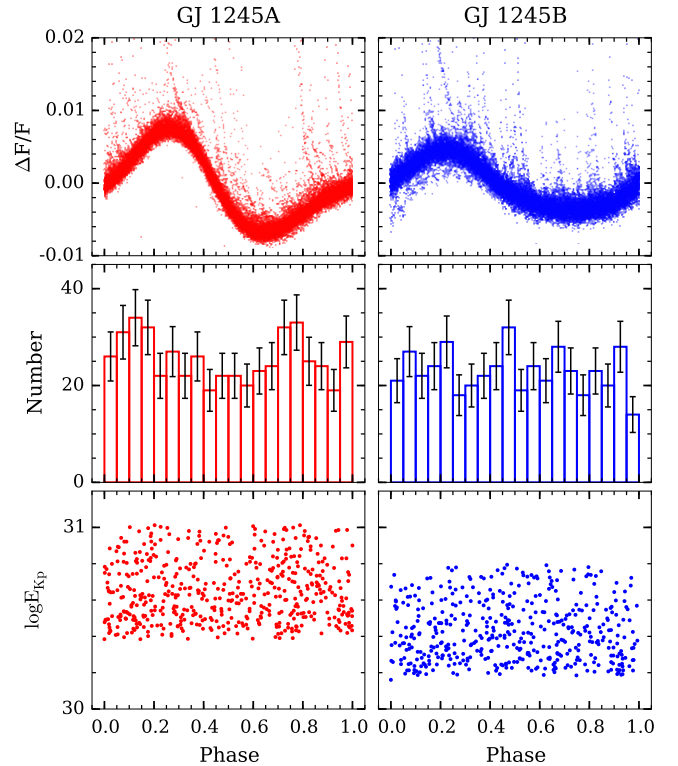


**Figure 10.** In the top panels, one month of short cadence separated light curves have been folded at the rotation period of each star. The number of flares (middle panels) and flare energy (bottom panels) for the 9 month dataset are plotted versus rotation phase. No correlations are seen with rotation phase.

ferential rotation on these three stars will be examined fully in a forthcoming paper (Davenport et al. 2014, in prep.). Equivalent widths for  $H\alpha$  are reported in Paper 1. These were converted to  $L_{H\alpha}/L_{bol}$  via multiplication by the  $\chi$  factor (Walkowicz et al. 2004), which is the ratio between the continuum flux near  $H\alpha$  and the bolometric flux.

Ideally, the flare rates among stars should be compared in terms of the luminosity emitted in flares relative to the bolometric luminosity,  $L_{fl}/L_{bol}$ , similar to the use of  $L_{H\alpha}/L_{bol}$  to compare the luminosity emitted in  $H\alpha$ . Observationally, we have determined the luminosity in flares relative to the luminosity in the Kepler bandpass,  $L_{fl}/L_{Kp}$ . Conversion of  $L_{fl}/L_{Kp}$  to  $L_{fl}/L_{bol}$  requires knowing the color-dependent bolometric correction for the Kepler filter, which is being developed in a future work (Davenport et al. 2015, in prep.). We caution that the value of  $L_{fl}/L_{Kp}$ , and therefore  $L_{fl}/L_{bol}$ , depends on



the range of equivalent durations over which the energy distribution is integrated. These considerations must be taken into account when comparing different stars, especially those that differ significantly in spectral type.

Because GJ 1245 A and B are nearly the same color, we can neglect the bolometric correction, and compare their values of  $L_{fl}/L_{Kp}$  as representative of  $L_{fl}/L_{bol}$ . We find that GJ 1245A emits a slightly higher fraction of energy in flares, while Paper 1 found that GJ 1245B emits a slightly higher fraction of energy in H $\alpha$  emission. Interestingly, the values of  $L_{fl}/L_{Kp}$  and  $L_{H\alpha}/L_{bol}$  are comparable for the range of flare equivalent durations we have considered. The scatter in  $L_{H\alpha}/L_{bol}$  for stars of the same spectral type (West et al. 2011) easily accounts for the difference between the A and B components. A similar scatter in  $L_{fl}/L_{Kp}$  is likely also present. We therefore do not find a correlation of activity parameters with rotation rate in the GJ 1245 AB system. From the measured rotation periods, and assuming radii of  $0.15 R_{\odot}$ , GJ 1245 A and B have rotational velocities of 11 and 29 km/s, respectively. This well above the threshold velocity of  $\sim 4$  km/s, where Mohanty & Basri (2003) found no correlation between rotation rate and activity for stars of this spectral type.

If we compare GJ 1245 A and B to GJ 1243, we find that GJ 1243 has the largest value of  $L_{fl}/L_{Kp}$ , with a trend of increasing  $L_{fl}/L_{Kp}$  with  $L_{Kp}$ . Lacy et al. (1976) found the opposite trend in the  $U$  and  $B$  bands, although the values of  $L_{fl,U}/L_U$  and  $L_{fl,B}/L_B$  were 1 – 3 orders of magnitude larger than what we measure in the Kepler bandpass. This underlines the importance of converting measures of  $L_{fl}$  taken in different bandpasses to  $L_{fl}/L_{bol}$ . Future work (Davenport et al. 2015, in prep.) will apply the flare light curve template presented in Paper 2 to understand the changes in relative flare luminosities in different bandpasses.

The flare energy distributions of all three stars have values of  $\alpha \approx 2$ . This is relevant to studies of the Sun, as the heating of the corona could be attributed to flares if  $\alpha > 2$  for the solar flare energy distribution at lower energies (Schrijver et al. 2012). However, Paper 2 found that the FFD of GJ 1243 had a shallower slope (smaller  $\alpha$ ) at lower energies, and that fewer low energy flares were observed than predicted by a power law slope with  $\alpha \approx 2$ . The flare samples for GJ 1245 A and B are incomplete below our signal to noise threshold. We therefore cannot say whether the stars flare less frequently at lower energies than predicted by the power law, or whether those flares occurred and were simply not detected due to noise.

For GJ 1245 A and B, the number of flares and flare energies show no correlation with rotation phase. The same was observed for GJ 1243 in Paper 1. This is consistent with a scenario where many small flaring regions are distributed uniformly with longitude, while the long lived spot features originate from large, axisymmetric poloidal magnetic fields, as seen in spectropolarimetric Doppler imaging of GJ 1245 B (Morin et al. 2010).

In agreement with previous observations (Collier Cameron 2007) and models (Küker & Rüdiger 2011), the amount of differential rotation increases with decreasing rotation rate. The fastest rotator, GJ 1245 A, shows the least differential rotation, and likely rotates as a nearly solid body. The slowest rotator, GJ 1245 B, shows the

greatest differential rotation, while the differential rotation of GJ 1243 is intermediate between GJ 1245 A and B. This is among the first observational constraints placed on the effect of rotation rate on differential rotation for M dwarfs, and in the case of GJ 1245 A and B, perhaps the first constraints for objects of the same age.

Our starspot and flare results are among the most detailed for an M dwarf multiple system, and involved an extensive analysis of the Kepler target pixel data. We emphasize the importance of the pixel data, both for the wealth of information they contain, and as a cautionary example of CCD non-linearity and saturation. Other investigations of impulsive phenomena using Kepler may encounter similar effects. In the broader context of stellar activity, these results contribute significantly to the existing dataset for fully convective M dwarfs. Together with other results from the Kepler program, they will help constrain the effects of age and rotation rate on stellar activity.

This work was supported by Kepler Cycle 2 GO grant NNX11AB71G and Cycle 3 GO grant NNX12AC79G. JCL acknowledges the support of the Washington Research Foundation and the University of Washington Provost’s Initiative in Data-Intensive Discovery. JRAD acknowledges support from NASA ADP grant NNX09AC77G. JRAD and SLH acknowledge support from NSF grant AST13-11678. SLH acknowledges support from NSF grant AST08-07205.

This paper includes data collected by the Kepler mission. Funding for the Kepler mission is provided by the NASA Science Mission directorate. Some of the data presented in this paper were obtained from the Mikulski Archive for Space Telescopes (MAST). STScI is operated by the Association of Universities for Research in Astronomy, Inc., under NASA contract NAS5-26555. Support for MAST for non-HST data is provided by the NASA Office of Space Science via grant NNX13AC07G and by other grants and contracts

This paper made use of PyKE (Still & Barclay 2012), a software package for the reduction and analysis of Kepler data. This open source software project is developed and distributed by the NASA Kepler Guest Observer Office. We thank Todd Henry and Fritz Benedict for sharing the orbital parameters for GJ 1245AC prior to publication. We would like to acknowledge the observing proposal of Steve Howell, under which the NOAO archived 2011 observation on the WIYN 0.9m was made.

## REFERENCES

- Browning, M. K. 2008, *ApJ*, 676, 1262  
 Browning, M. K., Basri, G., Marcy, G. W., West, A. A., & Zhang, J. 2010, *AJ*, 139, 504  
 Bryson, S. T., Tenenbaum, P., Jenkins, J. M., et al. 2010, *ApJ*, 713, L97  
 Chabrier, G., & Baraffe, I. 1997, *A&A*, 327, 1039  
 Christiansen, J. L., Jenkins, J. M., Caldwell, D. A., et al. 2013, *Kepler Data Characteristics Handbook (KSCI-19040-004)*  
 Collier Cameron, A. 2007, *Astronomische Nachrichten*, 328, 1030  
 Contadakis, M. E. 1995, *A&A*, 300, 819  
 Cutri, R. M., Skrutskie, M. F., van Dyk, S., et al. 2003, *VizieR Online Data Catalog*, 2246, 0  
 Dahn, C. C., Harrington, R. S., Riepe, B. Y., et al. 1976, *Publications of the U.S. Naval Observatory Second Series*, 24, 1  
 Davenport, J. R. A., Hawley, S. L., Hebb, L., et al. 2014, *ApJ*, 797, 122

- Delfosse, X., Forveille, T., Perrier, C., & Mayor, M. 1998, *A&A*, 331, 581
- Dieterich, S. B., Henry, T. J., Golimowski, D. A., Krist, J. E., & Tanner, A. M. 2012, *AJ*, 144, 64
- Dobler, W., Stix, M., & Brandenburg, A. 2006, *ApJ*, 638, 336
- Fanelli, M. N., Jenkins, J. M., Bryson, S. T., et al. 2011, *Kepler Data Processing Handbook (KSCI-19081-001)*
- Gizis, J. E., Burgasser, A. J., Berger, E., et al. 2013, *ApJ*, 779, 172
- Güdel, M. 2004, *A&A Rev.*, 12, 71
- Harrington, R. S. 1990, *AJ*, 100, 559
- Hawley, S. L., Davenport, J. R. A., Kowalski, A. F., et al. 2014, *ApJ*, 797, 121
- Hawley, S. L., Gizis, J. E., & Reid, I. N. 1996, *AJ*, 112, 2799
- Henry, T. J., Franz, O. G., Wasserman, L. H., et al. 1999, *ApJ*, 512, 864
- Hilton, E. J. 2011, PhD thesis, University of Washington
- Hosey, A. D., Henry, T. J., Jao, W. C., et al. 2014, *AJ* submitted
- Hunt-Walker, N. M., Hilton, E. J., Kowalski, A. F., Hawley, S. L., & Matthews, J. M. 2012, *PASP*, 124, 545
- Kelly, B. C. 2007, *ApJ*, 665, 1489
- Küker, M., & Rüdiger, G. 2011, *Astronomische Nachrichten*, 332, 933
- Lacy, C. H., Moffett, T. J., & Evans, D. S. 1976, *ApJS*, 30, 85
- McQuillan, A., Mazeh, T., & Aigrain, S. 2014, *ApJS*, 211, 24
- Mohanty, S., & Basri, G. 2003, *ApJ*, 583, 451
- Morin, J., Donati, J.-F., Petit, P., et al. 2010, *MNRAS*, 407, 2269
- Reid, I. N., Cruz, K. L., Allen, P., et al. 2004, *AJ*, 128, 463
- Schrijver, C. J., Beer, J., Baltensperger, U., et al. 2012, *Journal of Geophysical Research (Space Physics)*, 117, 8103
- Skumanich, A. 1972, *ApJ*, 171, 565
- Smith, J. C., Stumpe, M. C., Van Cleve, J. E., et al. 2012, *PASP*, 124, 1000
- Still, M., & Barclay, T. 2012, *PyKE: Reduction and analysis of Kepler Simple Aperture Photometry data*, astrophysics Source Code Library, ascl:1208.004
- Thompson, S. E., & Fraquelli, D. A. 2014, *Kepler Archive Manual (KDMC-10008-005)*
- van Altena, W. F., Lee, J. T., & Hoffleit, D. 1995, *VizieR Online Data Catalog*, 1174, 0
- Van Cleve, J., Caldwell, D., Thompson, R., et al. 2009, *Kepler Instrument Handbook (KSCI-19033-001)*
- Walkowicz, L. M., Hawley, S. L., & West, A. A. 2004, *PASP*, 116, 1105
- West, A. A., Morgan, D. P., Bochanski, J. J., et al. 2011, *AJ*, 141, 97